PCCP

ROYAL SOCIETY OF CHEMISTRY

PAPER

View Article Online
View Journal | View Issue

Check for updates

Cite this: *Phys. Chem. Chem. Phys.*, 2021, **23**, 11327

Received 12th March 2021,
Accepted 16th April 2021

DOI: 10.1039/d1cp01120k

rsc.li/pccp

High oxide-ion conductivity in acceptor-doped Bi-based perovskites at modest doping levels†

Linhao Li,[a] Joe Kler,[b] Anthony R. West,[a] Roger A. De Souza[b] and Derek C. Sinclair*[a]

A combination of impedance spectroscopy, time-of-flight secondary ion mass spectrometry and literature data are used to show that, (i) the bulk oxide ion conductivity of A-site, alkaline earth-doped $BiFeO_3$ (BF) is independent of the ionic radius of the alkaline earth ion (Ca, Sr, Ba) and, (ii) despite very different A-site environments in $(Na_{1/2}Bi_{1/2})TiO_3$ and BF, similar high levels and optimisation of bulk oxide ion conductivity in these Bi-based tilted perovskites is achieved at modest acceptor doping levels of ~1–10%. These results clearly demonstrate that optimisation of oxide ion conductivity in these materials requires concepts beyond a simple crystallochemical approach based on matching the ionic radii of acceptor dopant and host lattice ions.

Introduction

ABO_3 perovskite-based oxides have been widely explored for many decades due to their diverse range of functional properties. This spans from Ti^{4+} (d^0)-containing polar dielectrics such as ferroelectric $BaTiO_3$[1] and piezoelectric $Pb(Zr,Ti)O_3$[2] to Fe^{3+} (d^5)-containing multiferroic $BiFeO_3$[3] and mixed Cu^{2+} (d^9) and Cu^{3+} (d^8)-containing high temperature superconductors such as $YBa_2Cu_3O_7$.[4] Oxide-ion conductivity is another well-known phenomenon to occur in the perovskite lattice and many acceptor-doped phases have been investigated for the development of electrolytes and/or electrode materials in applications such as Solid Oxide Fuel Cells (SOFCs), *e.g.* Sr- and Mg-doped $LaGaO_3$ (LSGM)[5] and Sr- and Co-doped $LaFeO_3$ (LSCF),[6] respectively. De Souza has collated a wide range of diffusion data on oxygen vacancies in perovskites *via* Time-of-Flight Secondary Ion Mass Spectrometry (ToF-SIMS) and suggested that there may be a limit for such diffusion in a simple cubic perovskite lattice.[7] In 2014 we reported high levels of oxide-ion conductivity in undoped and lightly Mg-acceptor doped $Na_{1/2}Bi_{1/2}TiO_3$ (NBT).[8] Further attempts to increase the oxide-ion conductivity in NBT met with limited success despite the variety of A- and B-site acceptor dopants available.[9] A maximum enhancement of less than one order of magnitude was achieved using typically <2 at% of either A-site Sr (or Ca) or B-site Mg dopants.[9] The conductivity maximum was in good agreement with the model of an oxygen-vacancy diffusivity limit proposed by De Souza.[7]

The discovery of high levels of oxide ion conduction in NBT was unexpected as it had been investigated primarily as a Pb-free piezoelectric material.[10] NBT has a rather complex crystal structure, with Na and Bi disordered on the A-site and ferroelectricity arising from dipoles associated with Bi- and Ti-displacements.[11,12] The room temperature structure is reported as either rhombohedral (space group $R3c$)[11] or monoclinic (Cc),[13] with co-existence of rhombohedral (R) and tetragonal (space group $P4bm$) polymorphs over a range of temperatures (typically ~255 to 400 °C), before becoming fully tetragonal (T) and then finally cubic at and above ~520 °C. The activation energy (E_a) for the oxide-ion conductivity changes on heating from ~0.8 to 0.4 eV at ~325–350 °C[8] and has been attributed to changes in volume fraction of co-existing R and T polymorphs.[14]

Various modelling methods and studies[15–17] have been tried to improve understanding of structure–property relations in NBT with respect to oxide ion conductivity and some trends have emerged. For example, migration energy of oxide ions *via* saddle points in the lattice associated with two A-site cations and a B-site cation are lowest for Bi located on both A-sites compared to either Na or mixed Na–Bi A-site occupation.[15] Experimental E_a values agree well with simulations for Na–Bi as the A-site saddle point cations, in good agreement with the (average) disordered arrangement of Na and Bi on the A-sites in NBT. The influence of polymorphism on E_a[16] and ordering of Na^+ and Bi^{3+} ions on oxygen tracer diffusion[17] have given further mechanistic insights into the oxide ion conductivity. A complete explanation is still lacking however, owing mainly

---

[a] *Department of Materials Science and Engineering, University of Sheffield, Sheffield, S1 3JD, UK. E-mail: d.c.sinclair@sheffield.ac.uk*

[b] *Institute of Physical Chemistry, RWTH Aachen University, Landoltweg 2, 52056 Aachen, Germany*

† Electronic supplementary information (ESI) available. See DOI: 10.1039/d1cp01120k

to the complexity of the crystallography and polymorphism of NBT.

These studies on NBT have led to the suggestion that other Bi-based perovskites may show similar behaviour. Unfortunately, very few Bi-based perovskites can be prepared under normal atmospheric conditions; most require high pressure synthesis such as $BiMO_3$: M = Al,[18] Sc,[19] Mn.[20] One notable exception is $BiFeO_3$ (BF) which has been widely studied as a multiferroic.[21] Its electrical properties that include mixed ionic–electronic and oxide ion conductivity in acceptor-doped BF, depend strongly on processing conditions.[22–27] High levels of oxygen permeability were reported in Sr-doped BF[23] and Impedance Spectroscopy (IS) measurements showed the level of oxide ion conductivity in Ca-doped BF (with 3, 5 and 30 at% replacement of Ca for Bi on the A-site) is as high as that observed in the well-known fluorite-based solid electrolyte, yttrium-stabilised zirconia, 8YSZ.[24] Ionic conduction was explained on the basis of A-site Ca-doping compensated by oxygen vacancy creation $\left(V_O^{\bullet\bullet}\right)$ as follows (using Kröger–Vink notation):

$$2\mathrm{CaO} \xrightarrow{\mathrm{Bi_2O_3}} 2\mathrm{Ca}'_{\mathrm{Bi}} + 2\mathrm{O}_\mathrm{O}^\times + \mathrm{V}_\mathrm{O}^{\bullet\bullet} \qquad (1)$$

When processed in air, the oxygen vacancies are partially filled by uptake of oxygen from the atmosphere on cooling. This creates electron holes (h) by the following reaction:

$$\mathrm{V}_\mathrm{O}^{\bullet\bullet} + \frac{1}{2}\mathrm{O}_2(\mathrm{g}) \rightarrow \mathrm{O}_\mathrm{O}^\times + 2\mathrm{h}^\bullet \qquad (2)$$

and gives rise to high levels of p-type conductivity with $E_a \sim$ 0.27–0.45 eV. Chemically, the electronic conduction was inferred to arise from partial oxidation of Fe^{3+} to Fe^{4+} ions and/or O^{2-} to O^- ions. Oxidation was suppressed by annealing in N_2 at 800 °C, with subsequent cooling in N_2. Impedance measurements in N_2 showed a single arc in impedance complex plane, Z^*, plots with a capacitance of a few pF cm^{-1} for $Bi_{0.7}Ca_{0.3}FeO_{3-\delta}$ that was attributed to a bulk/grain response and a low frequency Warburg impedance that was taken as evidence of oxide ion conductivity. The conductivity of such N_2-processed ceramics was several orders of magnitude lower than that of ceramics processed in air and E_a increased substantially to ~0.8–1.0 eV. The bulk oxide ion conductivity was relatively insensitive to the level of Ca-doping between 3 and 30 at% on the A-site. This insensitivity to composition was attributed to reduction in mobile ion concentration by vacancy-acceptor dopant association, thus behaving as a weak electrolyte.

Zhang *et al.*[17] performed molecular dynamics simulations to calculate the oxygen diffusion coefficient for several A- and B-site acceptor and isovalent dopants in rhombohedral BF. This study revealed significant limitations in applying widely-used, empirical crystallochemical relations to maximise oxide ion diffusivity in perovskites when the acceptor dopants are close in size to that of host cations. Consequently, to predict the macroscopic level of oxide ion transport and choose an optimum dopant remains a challenge.

In this study, we use IS on N_2-annealed samples to show that A-site acceptor-doping $BiFeO_3$ by 5 at% Ba displays similar behaviour and levels of bulk oxide ion conduction to that reported for N_2-annealed 3–30 at% Ca-doped BF.[24] The presence of a high capacitance, low frequency spike in Z^* plots for the N_2-annealed samples is taken as an indicator of dominant oxide-ion conductivity. Samples subjected to $^{18}O/^{16}O$ exchange at 500 and 600 °C and subsequent ToF-SIMS analysis yielded high tracer diffusion coefficients, D^*. The Nernst–Einstein equation was used to convert D^* data into bulk conductivity values, giving good agreement with extrapolated values obtained at lower temperatures by IS and provides direct evidence for oxide ion conductivity. Interestingly, the values of ionic conductivity and E_a are similar to those of optimised, acceptor-doped NBT. This indicates that, despite the complexities of oxide-ion migration pathways in the non-cubic, Bi-based NBT and BF perovskites, conductivity optimisation may be achieved by modest levels, ~1–10 at%, of A-site acceptor doping by alkaline earth (AE) elements.

Experimental

Three series of AE-doped BF ceramics were prepared (AE = Ca, Sr and Ba). Full impedance data are given for AE = Ba (5 at%) but the results for AE = Ca, Sr showed similar characteristics and for conciseness only bulk conductivity values at 200 °C for all ceramics are given (see Fig. 6(b)). $BiFeO_3$ (BF) and $Bi_{0.95}Ba_{0.05}FeO_{2.975\pm\delta}$ (BF-Ba) ceramics were prepared by solid state reaction of Bi_2O_3 (99.9%, Acros Organics), Fe_2O_3 (99.9%, Sigma-Aldrich) and $BaCO_3$ (99%, Sigma-Aldrich), as appropriate. All reagents were pre-dried before weighing and appropriate mixtures of powders were ball milled. Calcination was carried out at 800 °C for 2 h. Pellets were sintered at 860–925 °C for 1 h depending on composition. For IS measurements, Au paste was coated (850 °C for 2 h) on opposite faces of the pellets. To measure oxide ion conductivity, Au-coated samples were annealed at 800 °C in N_2 for 6 h and cooled to room temperature in N_2 to minimise oxidation and therefore p-type electronic conductivity. IS measurements for N_2-annealed samples were made in 5% H_2, 95% N_2 atmosphere.

Phase purity was examined by X-ray diffraction (XRD) using a high-resolution STOE STADI-P diffractometer equipped with a linear position sensitive detector and Cu Kα_1 radiation. Ceramic microstructure and compositional analysis were analysed using a scanning electron microscope (SEM) Philips XL 30S FEG with an Oxford Link ISIS energy dispersive X-ray (EDS) detector. Variable temperature IS measurements were made in either a non-inductively wound tube furnace or an Oxford cryodrive 1.5 system using Solartron 1260, Solartron Modulab and Agilent E4980A instrumentation. IS data were corrected for sample geometry (thickness/area of pellet) and analysed using ZView software.

Isotope exchange experiments were carried out by first equilibrating samples in O_2 of normal isotopic abundance at the chosen temperature (500 °C or 600 °C) and oxygen partial pressure, pO_2 of 200 mbar. The duration of the equilibration was ten times that of the exchange, $t_{eq} = 10t_{ex}$. The samples were quenched to room temperature, reannealed in ^{18}O-enriched O_2 (the isotope fraction in the gas phase being $n_g^* = 0.97$) at the same temperature and pO_2 for a time t_{ex}, and quenched again to room temperature.[28] The long penetration depths required use of the line scan technique.[29] Exchanged samples were cut perpendicular to the original surface, the revealed cross-section was polished and then analysed[30] using a ToF-SIMS IV machine equipped with a ToF-SIMS V analyser (IONTOF GmbH, Münster, Germany). The surface was cleaned initially by sputtering with a beam of 2 keV Cs^+ ($I_{Cs^+} = 100$ nA) rastered over 800 μm × 800 μm. Secondary ion images were acquired with a beam of 25 keV Ga^+ operated in fast imaging mode (pulse time 100 ns, nominal mass resolution, submicron beam diameter), rastered over 500 μm × 500 μm. Negative secondary ions were detected with a ToF cycle time of 75 μs.

The chosen experimental conditions for isotope exchange—surface-limited isotope exchange from a large volume of gas into a semi-infinite medium—result in the following solution to the diffusion equation:[31]

$$n_r^*(x) = \mathrm{erfc}\left(\frac{x}{2\sqrt{D^* t_{ex}}}\right) - \exp\left(\frac{k^*}{D^*}x + \frac{k^{*2}}{D^*}t_{ex}\right) \cdot \mathrm{erfc}\left(\frac{x}{2\sqrt{D^* t_{ex}}} + k^*\sqrt{\frac{t_{ex}}{D^*}}\right). \tag{3}$$

This equation expresses the isotope fraction, corrected for gas-phase and background isotope fractions, as a function of position in the solid, x, in terms of the tracer diffusion coefficient of oxygen, D^*, and the oxygen surface exchange coefficient, k^*.

Results and discussion

XRD patterns at room temperature for undoped BF and BF-Ba ceramics are shown in Fig. S1 (ESI†); both indexed as rhombohedral (space group *R*3*cH*) perovskites. A small amount of $Bi_2Fe_4O_9$ (space group *Pbam*) was detected in BF ceramics whereas BF-Ba ceramics appeared to be phase-pure. Refined lattice parameters were $a = 5.572(1)$ Å and $c = 13.852(3)$ Å for BF and $a = 5.575(2)$ Å and $c = 13.840(1)$ Å for BF-Ba. An SEM image shows the grain size in BF-Ba ceramics to be in the range of 0.5 to 2 μm, Fig. S2 (ESI†). The average relative density of sintered BF and BF-Ba pellets was 84 and 92%, respectively. For completeness, the relative density values of all AE-doped ceramics used in Impedance measurements are given in Fig. S3 (ESI†).

IS data were analysed using a combination of Z^* plots, combined spectroscopic plots of the imaginary components of impedance and electric modulus (Z'', M'') and spectroscopic plots of the real component of the capacitance (C'). Z^* plots were used to overview the dominant impedances in the samples and seek evidence for oxygen diffusion/electrode effects in low frequency data at higher temperatures.[24] Z'', M'' plots were used to identify unequivocally the bulk response and extract bulk conductivity, σ_b, data from M'' peak maxima.[32] C' plots gave capacitance values for the different impedance components.

IS data for a sample that was N_2-annealed, BF-Ba(N_2), and subsequently measured in 5% H_2, 95% N_2, are shown in Fig. 1. Z^* data show two broad, depressed arcs with an inclined spike at lowest frequencies, Fig. 1(a) and (b). Z'', M'' plots in Fig. 1(c) and (d) show a high frequency M'' peak that is coincident with the high frequency Z'' peak and therefore, the high frequency Z^* arc represents the bulk response. C' data in Fig. 1(e) and (f) show a high frequency plateau with a value of approximately

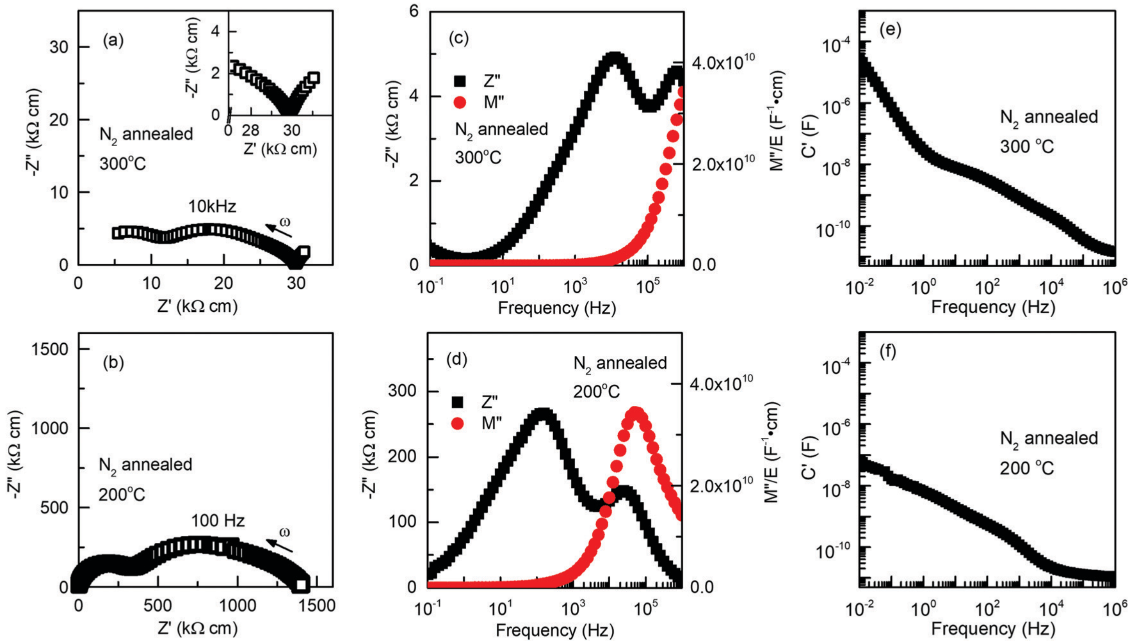

Fig. 1 Z^* plots, combined Z'' and M'' spectroscopic plots and C' plot for N_2 annealed $Bi_{0.95}Ba_{0.05}FeO_{2.975}$ ceramics at 300 °C (a), (c) and (e), 200 °C (b), (d) and (f), respectively.

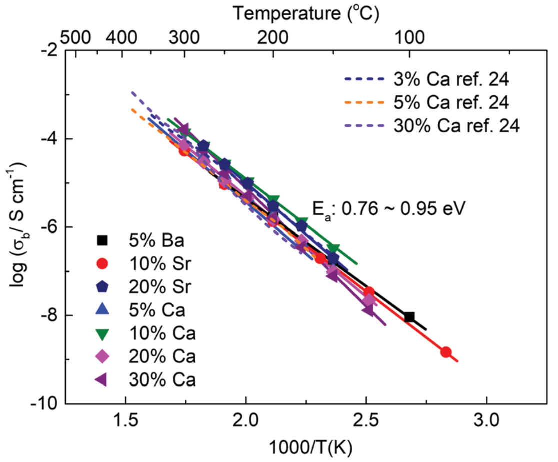

Fig. 2 Arrhenius plot of σ_b for N_2 annealed Ba/Sr/Ca-doped BF ceramics with Ca-doped BF data from ref. 24.

10 pF cm^{-1} representing the bulk response. At lower frequencies, a broad dispersion terminating in a plateau at about 10 nF cm^{-1} is seen and is attributed to a combination of a grain boundary impedance and the sample-electrode impedance associated with oxygen transfer across the interface. At the lowest frequencies, the C' data show a further increase to values as high as 20 μF cm^{-1} and are attributed to the onset of a Warburg impedance associated with diffusion of oxygen molecules towards/away from the sample-electrode interfaces.

These C' data demonstrate clearly that the BF-Ba(N_2) sample is an oxide ion conductor. Our focus here is on the bulk response and therefore, detailed circuit fitting to extract grain boundary and electrode impedances has not been carried out. This IS response is similar to that reported for Ca-doped BF under similar annealing conditions,[24] which was also attributed to oxide ion conduction. An Arrhenius plot of σ_b data obtained from M'' spectra for BF-Ba(N_2) is shown in Fig. 2 together with σ_b data obtained for other AE-doped BF samples prepared in this study and also σ_b data reported for Ca doped BF by Maso and West.[24] The Arrhenius plots for all of these compositions are very similar. E_a's are in the range 0.69–0.95 eV, similar to those for good oxide ion conductors such as 8YSZ.

Results for BF-Ba processed in air, BF-Ba(air), are shown in Fig. 3. There are two main differences from the BF-Ba(N_2) data

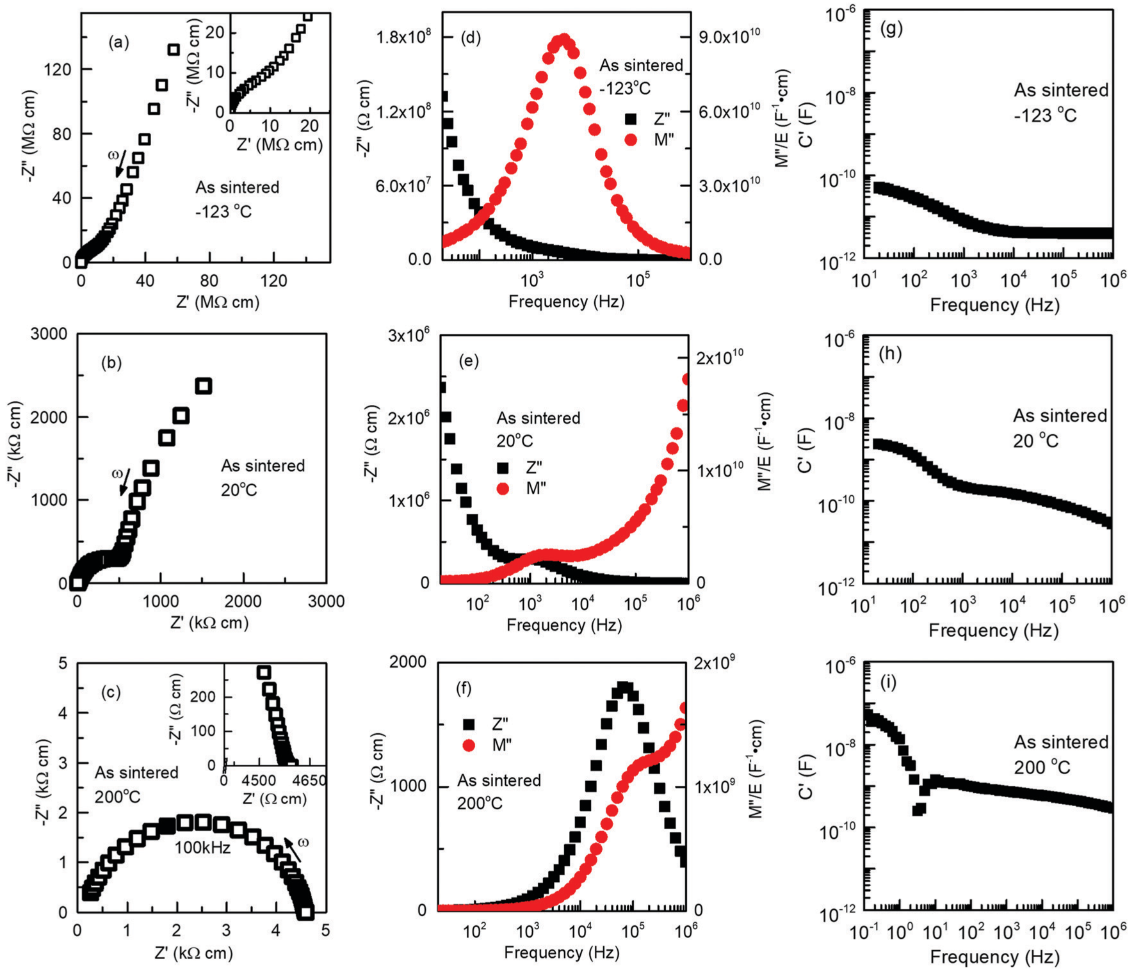

Fig. 3 Z^* plots, combined Z'' and M'' spectroscopic plots and C' plots for as sintered $Bi_{0.95}Ba_{0.05}FeO_{2.975}$ ceramics at −123 °C (a), (d) and (g), 20 °C (b), (e) and (h), and 200 °C (c), (f) and (i), respectively.

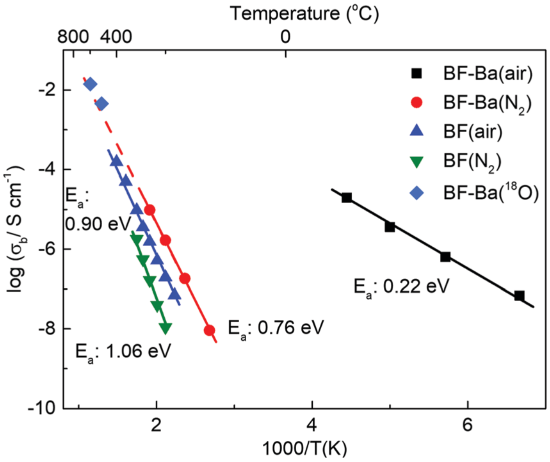

Fig. 4 Arrhenius plot of bulk conductivity, σ_b, *versus* reciprocal temperature for as sintered and N_2 annealed $Bi_{0.95}Ba_{0.05}FeO_{2.975}$ ceramics. σ_b calculated from ToF-SIMS ^{18}O diffusion data are shown as BF-Ba ^{18}O symbols. The dashed line is an extrapolation to higher temperatures of σ_b for BF-Ba N_2.

sets, Fig. 1. First, the BF-Ba(air) resistances are much lower and consequently, measurements at sub-ambient temperatures were required to show all the features in the Z^* plots, Fig. 3(a–c), and access the high frequency, bulk M'' peak (d). Second, the prominent low frequency dispersion in C' data was largely absent, with values smaller than 10 nF cm^{-1}, Fig. 3(i). It is concluded that BF-Ba(air) is predominantly an electronic conductor, therefore. The oxide ion conductivity seen in the BF-Ba(N_2) data sets is, of course, still present in BF-Ba(air) but is swamped by the much higher electronic conductivity. The only difference between the two samples is their heat treatment history; since BF-Ba(air) was treated in an atmosphere of relatively, much higher pO_2, the samples had absorbed O_2 according to eqn (2) and therefore, their observed bulk electronic conductivity was p-type.

Data for σ_b obtained from the bulk M'' peaks are shown in Fig. 4, together with σ_b data for BF-Ba(N_2). The remarkable change in bulk conductivity properties with atmosphere of BF-Ba indicates that, in a plot of σ_b *vs.* pO_2, the samples would be at the cross-over from the electrolytic domain, BF-Ba(N_2) to the p-type domain, BF-Ba(air). The conductivities for the two domains differ by several orders of magnitude, especially at low temperatures because of their different E_a. The transport number of oxide ions, t_o, in the p-type domain is very small but temperature-dependent and can be estimated from the ratio of the conductivities if it is assumed that the level of oxide ion conductivity is relatively similar in the two samples. For example, at room temperature, the ratio of the extrapolated conductivity values is $\sim 10^5:1$ and therefore, t_o is estimated as $\sim 1 \times 10^{-5}$ in BF-Ba(air).

The behaviour of acceptor-doped BF and NBT materials towards increasing pO_2 are very different. For BF materials, the onset of p-type behaviour occurs very rapidly if air is not excluded from BF-Ba(N_2) samples, for instance during IS measurements. For NBT samples, however, the electrolytic domain extends to much higher pO_2 and the materials are stable oxide ion conductors in air.[8,9] Both sets of materials contain oxygen vacancies but only BF-based materials absorb O_2 readily. The reason may be the ready availability of the Fe^{4+} state in BF, permitting easy activation of the Fe^{3+}/O_2 redox couple, whereas there is no corresponding couple associated with Ti^{4+} in NBT. The O^{2-}/O^- couple may also be involved but it is not obvious why this should be activated in BF but not in NBT. A third possibility is that higher levels of the valence band electronic states in BF involve cation–anion hybridisation associated with contributions from the Fe 3d and Bi 6s/6p (lone pair) orbitals as well as O 2p orbitals.[33] The p-type conductivity is an activated process, however, with E_a around 0.2 eV and therefore, the holes are localised rather than delocalised in a valence band.

ToF-SIMS measurements on BF-Ba ceramics that were exchange-annealed in 200 mbar O_2 at 500 and 600 °C revealed D^* values in the range $(1–5) \times 10^{-8}$ cm^2 s^{-1}, Fig. 5, with an ^{18}O penetration depth of $\sim$200 microns at 600 °C. As the grain size in BF-Ba ceramics is $\sim$0.5–2 μm, Fig. S2 (ESI†), the tracer species encounter numerous grains and grain boundaries. These D^* values are of the same order of magnitude as reported for Mg-doped NBT[8] and LSGM.[34]

The conductivity values calculated using the Nernst–Einstein equation on data from D^* at 500 and 600 °C for BF-Ba are shown

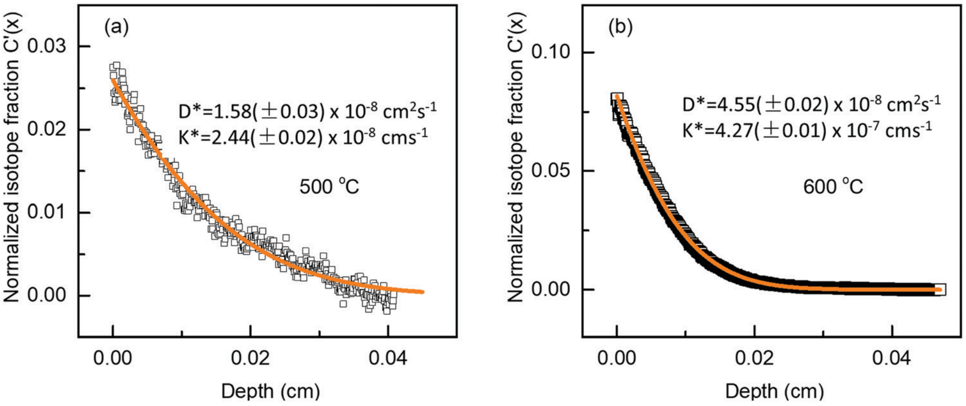

Fig. 5 ^{18}O diffusion profiles for $Bi_{0.95}Ba_{0.05}FeO_{2.975}$ ceramics after exchange at (a) 500 °C for 14 670 s and (b) 600 °C for 1496 s. Orange lines represent the best fit.

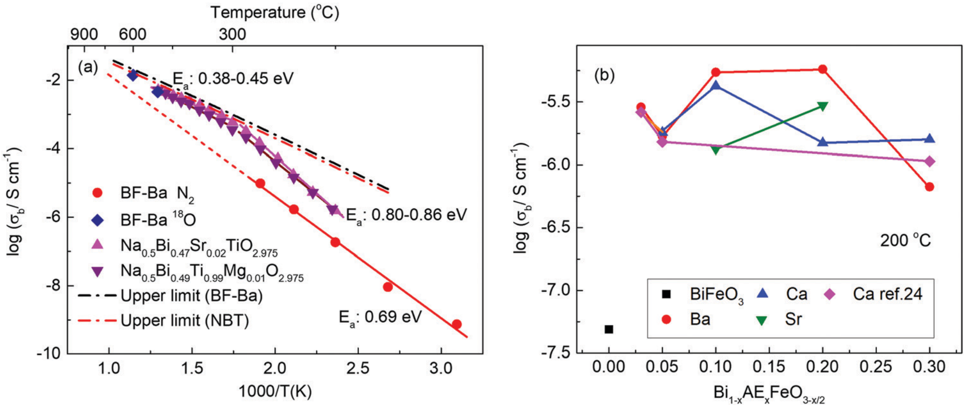

Fig. 6 (a) Arrhenius plot of σ_b for N_2 annealed $Bi_{0.95}Ba_{0.05}FeO_{2.975}$ ceramics and air processed $Na_{0.5}Bi_{0.47}Sr_{0.02}TiO_{2.975}$ and $Na_{0.5}Bi_{0.49}Ti_{0.99}Mg_{0.01}O_{2.975}$ ceramics obtained from impedance spectroscopy data. The dashed line is an extrapolation to higher temperatures of σ_b for BF-Ba N_2. σ_b calculated from ToF-SIMS ^{18}O diffusion data are shown as BF-Ba ^{18}O symbols. The upper limits of σ_b for doped NBT and BF (both with an oxygen deficiency of 0.025) calculated from the Nernst–Einstein equation using the oxygen-vacancy diffusivity limit in a cubic perovskite lattice proposed in ref. 7 (dash-dot line) are also presented. (b) Isothermal σ_b values at 200 °C for N_2 annealed $BiFeO_3$, $Bi_{1-x}Ba_xFeO_{3-x/2}$, $Bi_{1-x}Sr_xFeO_{3-x/2}$ and $Bi_{1-x}Ca_xFeO_{3-x/2}$ (from this study and ref. 24).

in Fig. 4. These data points are in reasonable agreement with extrapolated σ_b values obtained from IS data for BF-Ba(N_2) and confirm the presence of high levels of oxide-ion conduction in BF-Ba ceramics. It also implies that grain boundaries in BF-Ba are not severely blocking to oxygen transport, otherwise a large discrepancy between bulk conductivity and diffusion data may be anticipated.

For comparison, σ_b based on the oxygen-vacancy diffusion limit from ref. 7 and σ_b from optimised Mg/Sr-doped NBT obtained from IS measurements, together with data measured here, are summarised in Fig. 6(a). Isothermal values of σ_b at 200 °C for different alkaline earth doped BF samples prepared in this study and ref. 24 are shown in in Fig. 6(b). The similarity in magnitudes of σ_b and E_a in all of these Bi-based perovskites (in a range where the R polymorph is present) is remarkable given the different A-site environments in NBT and BF and the different types and levels of acceptor-dopants. This demonstrates that optimisation of oxide-ion conductivity in these Bi-based tilted perovskites requires concepts beyond a simple crystallochemical approach based on matching the ionic radii of acceptor dopant and host ions, as suggested by Zhang *et al.*[17] Octahedral tilting, variations in local structure and acceptor-vacancy trapping can all potentially influence the concentration and mobility of the (mobile) oxide ions and further studies are required to elucidate the mechanism(s) responsible.

Conflicts of interest

The authors declare no conflict of interest.

Acknowledgements

L. L. and D. C. S. thank the EPSRC for funding (EP/L027348/1 and EP/L017563/1). J. K. and R. A. D. S. acknowledge funding from the German Research Foundation (DFG) within the framework of the Collaborative Research Centre SFB 917 ‘‘Nanoswitches’’.

References

1 H. D. Megaw, Crystal structure of barium titanate, *Nature*, 1945, **155**, 484–485.
2 B. Jaffe, *US Pat.*, 2708244, 1955.
3 J. B. N. J. Wang, J. B. Neaton, H. Zheng, V. Nagarajan, S. B. Ogale, B. Liu, D. Viehland, V. Vaithyanathan, D. G. Schlom, U. V. Waghmare and N. A. Spaldin, Epitaxial $BiFeO_3$ Multiferroic Thin Film Heterostructures, *Science*, 2003, **299**, 1719–1722.
4 M. K. Wu, J. R. Ashburn, C. Torng, P. H. Hor, R. L. Meng, L. Gao, Z. J. Huang, Y. Q. Wang and A. Chu, Superconductivity at 93 K in a New Mixed-Phase Y–Ba–Cu–O Compound System at Ambient Pressure, *Phys. Rev. Lett.*, 1987, **58**, 908.
5 T. Ishihara, H. Matsuda and Y. Takita, Doped $LaGaO_3$ Perovskite Type Oxide as a New Oxide Ionic Conductor, *J. Am. Chem. Soc.*, 1994, **116**, 3801–3803.
6 T. Ishihara, T. Yamada, H. Arikawa, H. Nishiguchi and Y. Takita, Mixed electronic-oxide ionic conductivity and oxygen permeating property of Fe-, Co- or Ni-doped LaGaO3 perovskite oxide, *Solid State Ionics*, 2000, **135**, 631–636.
7 R. A. De, Souza, Oxygen Diffusion in $SrTiO_3$ and Related Perovskite Oxides, *Adv. Funct. Mater.*, 2015, **25**, 6326–6342.
8 M. Li, M. J. Pietrowski, R. A. De Souza, H. Zhang, I. M. Reaney, S. N. Cook, J. A. Kilner and D. C. Sinclair, A family of oxide ion conductors based on the ferroelectric perovskite $Na_{0.5}Bi_{0.5}TiO_3$, *Nat. Mater.*, 2014, **13**, 31–35.
9 F. Yang, M. Li, L. Li, P. Wu, E. Pradal-Velázque and D. C. Sinclair, Optimisation of oxide-ion conductivity in acceptor-doped $Na_{0.5}Bi_{0.5}TiO_3$ perovskite: approaching the limit?, *J. Mater. Chem. A*, 2017, **5**, 21658–21662.

10 D. Damjanovic, N. Klein, J. Li and V. Porokhonskyy, What can be expected from lead-free piezoelectric materials?, *Funct. Mater. Lett.*, 2010, **3**, 5–13.

11 G. O. Jones and P. A. Thomas, Investigation of the structure and phase transitions in the novel A-site substituted distorted perovskite compound $Na_{0.5}Bi_{0.5}TiO_3$, *Acta Crystallogr., Sect. B: Struct. Sci.*, 2002, **58**, 168–178.

12 I. Levin and I. M. Reaney, Nano- and Mesoscale Structure of $Na_{1/2}Bi_{1/2}TiO_3$: A TEM Perspective, *Adv. Funct. Mater.*, 2012, **22**, 3445–3452.

13 E. Aksel, J. S. Forrester, J. L. Jones, P. A. Thomas, K. Page and M. R. Suchomel, Monoclinic crystal structure of polycrystalline $Na_{0.5}Bi_{0.5}TiO_3$, *Appl. Phys. Lett.*, 2011, **98**, 152901.

14 F. Yang, H. Zhang, L. Li, I. M. Reaney and D. C. Sinclair, High Ionic Conductivity with Low Degradation in A-Site Strontium-Doped Nonstoichiometric Sodium Bismuth Titanate Perovskite, *Chem. Mater.*, 2016, **28**, 5269–5273.

15 X. He and Y. Mo, Accelerated Materials Design of $Na_{0.5}Bi_{0.5}TiO_3$ Oxygen Ionic Conductors Based on First Principles Calculations, *Phys. Chem. Chem. Phys.*, 2015, **17**, 18035–18044.

16 K.-C. Meyer and K. Albe, Influence of phase transitions and defect associates on the oxygen migration in the ion conductor $Na_{1/2}Bi_{1/2}TiO_3$, *J. Mater. Chem. A*, 2017, **5**, 4368–4375.

17 H. Zhang, A. H. H. Ramadan and R. A. De Souza, Atomistic simulations of ion migration in sodium bismuth titanate (NBT) materials: towards superior oxide-ion conductors, *J. Mater. Chem. A*, 2018, **6**, 9116–9123.

18 A. A. Belik, T. Wuernisha, T. Kamiyama, K. Mori, M. Male, T. Nagai, Y. Matsui and E. Takayama-Muromachi, High-pressure synthesis, crystal structures, and properties of perovskite-like $BiAlO_3$ and pyroxene-like $BiGaO_3$, *Chem. Mater.*, 2006, **18**, 133–139.

19 A. A. Belik, S. Iikubo, K. Kodama, N. Igawa, S. I. Shamoto, M. Maie, T. Nagai, Y. Matsui, S. Y. Stefanovich, B. I. Lazoryak and E. Takayama-Muromachi, $BiScO_3$: centrosymmetric $BiMnO_3$-type oxide, *J. Am. Chem. Soc.*, 2006, **128**, 706–707.

20 T. Atou, H. Chiba, K. Ohoyama, Y. Yamaguchi and Y. Syono, Structure determination of ferromagnetic perovskite $BiMnO_3$, *J. Solid State Chem.*, 1999, **145**, 639–642.

21 G. Catalan and J. F. Scott, Physics and Applications of Bismuth Ferrite, *Adv. Mater.*, 2009, **21**, 2463–2485.

22 W.-T. Chen, A. J. Williams, L. Ortega-San-Martin, M. Li, D. C. Sinclair, W. Zhou and J. P. Attfield, Robust Antiferromagnetism and Structural Disorder in Bi_x-$Ca_{1-x}FeO_3$ Perovskites, *Chem. Mater.*, 2009, **21**, 2085–2093.

23 K. Brinkman, T. Iijima and H. Takamura, The oxygen permeation characteristics of $Bi_{1-x}Sr_xFeO_3$ mixed ionic and electronic conducting ceramics, *Solid State Ionics*, 2010, **181**, 53–58.

24 N. Masó and A. R. West, Electrical properties of Ca-doped $BiFeO_3$ ceramics: from p-type semiconduction to oxide-ion conduction, *Chem. Mater.*, 2012, **24**, 2127–2132.

25 M. Schrade, N. Masó, A. Perejón, L. A. Pérez-Maqueda and A. R. West, Defect chemistry and electrical properties of $BiFeO_3$, *J. Mater. Chem. C*, 2017, **5**, 10077–10086.

26 J. S. Lim, J. H. Lee, H. S. Park, R. Gao, T. Y. Koo, L. W. Martin, R. Ramesh and C. H. Yang, Ultrafast collective oxygen-vacancy flow in Ca-doped $BiFeO_3$, *NPG Asia Mater.*, 2018, **10**, 943–955.

27 H. Zhang and R. A. De Souza, Optimising oxygen diffusion in non-cubic, non-dilute perovskite oxides based on $BiFeO_3$, *J. Mater. Chem. A*, 2019, **7**, 25274–25278.

28 R. A. De Souza and R. J. Chater, Oxygen exchange and diffusion measurements: the importance of extracting the correct initial and boundary conditions, *Solid State Ionics*, 2005, **176**, 1915–1920.

29 S. Carter, A. Selcuk, R. J. Chater, J. Kajda, J. A. Kilner and B. C. H. Steele, Oxygen transport in selected nonstoichiometric perovskite-structure oxides, *Solid State Ionics*, 1992, **53**, 597–605.

30 R. A. De Souza, J. Zehnpfenning, M. Martin and J. Maier, Determining oxygen isotope profiles in oxides with Time-of-Flight SIMS, *Solid State Ionics*, 2005, **176**, 1465–1471.

31 J. Crank, *The mathematics of diffusion*, Oxford University Press, 1975.

32 J. T. S. Irvine, D. C. Sinclair and A. R. West, Electroceramics: characterization by impedance spectroscopy, *Adv. Mater.*, 1990, **2**, 132–138.

33 S. Li, J. Morasch, A. Klein, C. Chirila, L. Pintilie, L. Jia, K. Ellmer, M. Naderer, K. Reichmann, M. Gröting and K. Albe, Influence of orbital contributions to the valence band alignment of Bi_2O_3, Fe_2O_3, $BiFeO_3$, and $Bi_{0.5}Na_{0.5}TiO_3$, *Phys. Rev. B: Condens. Matter Mater. Phys.*, 2013, **88**, 045428.

34 C. Haavik, E. M. Ottesen, K. Nomura, J. A. Kilner and T. Norby, Temperature dependence of oxygen ion transport in Sr + Mg-substituted $LaGaO_3$ (LSGM) with varying grain sizes, *Solid State Ionics*, 2004, **174**, 233–243.